Thermal coupling potential of Solid Oxide Fuel Cells with metal hydride tanks: Thermodynamic and design considerations towards integrated systems

Andreas G. Yiotis[*], Michael E. Kainourgiakis, Lefteris I. Kosmidis, Georgia C. Charalambopoulou, Athanassios K. Stubos

Environmental Research Laboratory, NCSR 'Demokritos', 15310 Athens, Greece

HIGHLIGHTS

- We study the thermal coupling potential of SOFCs with metal hydride tanks.
- We propose an integrated system design for self-sustainable tank operation.
- We develop a numerical model for heat and mass transfer in the system.
- Thermal coupling is feasible at typical operating SOFC conditions.

ARTICLE INFO

ABSTRACT

We study the thermal coupling potential between a high temperature metal hydride (MH) tank and a Solid Oxide Fuel Cell (SOFC) aiming towards the design of an efficient integrated system, where the thermal power produced during normal SOFC operation is redirected towards the MH tank in order to maintain H_2 desorption without the use of external heating sources. Based on principles of thermodynamics, we calculate the energy balance in the SOFC/MH system and derive analytical expressions for both the thermal power produced during SOFC operation and the corresponding thermal power required for H_2 desorption, as a function of the operating temperature, efficiency and fuel utilization ratio in the SOFC, and the MH enthalpy of desorption in the tank. Based on these calculations, we propose an integrated SOFC/MH design where heat is transferred primarily by radiation to the tank in order to maintain steady-state desorption conditions. We develop a mathematical model for this particular design that accounts for heat/mass transfer and desorption kinetics in the tank, and solve for the dynamics of the system assuming MgH_2 as a storage material. Our results focus primarily on tank operating conditions, such as pressure, temperature and H_2 saturation profiles vs operation time.

© 2014 Elsevier B.V. All rights reserved.

1. Introduction

Considerable research has been invested in recent years towards the development of non-petroleum energy carriers for use both in mobile (transportation, portable devices etc) and stationary applications (backup and auxiliary power units, distributed electricity generation etc). In this direction, hydrogen has emerged as an attractive option due to its production from a variety of primary energy sources, its high energy content and clean exhaust product. Furthermore, the use of H_2 can significantly contribute to the successful penetration of renewable energy (RE) sources in the electricity grid, as it offers a promising alternative medium for RE storage, which could be subsequently used as a clean fuel for vehicles, as well as for distributed electricity production through the use of fuel cells, or even internal combustion engines, etc.

Efficient H_2 storage remains, however, a significant technological barrier towards the widespread application of hydrogen powered devices and vehicles, as the volumetric energy density of uncompressed hydrogen gas is very low. In this direction, metal hydrides (MHs) are being considered as promising hydrogen stores due to their inherent high gravimetric hydrogen content, and significant effort is devoted to the development of MH-based upscaled storage systems and their testing (in terms of storage capacity, charging/discharging kinetics, reversibility and cycling, etc.) at

different operating conditions [1,2]. As a matter of fact, commercial MH tanks became very recently available for stationary applications [3] building on the distinct advantages of MgH_2, i.e. its high reversible gravimetric capacity (7.6% w/w), flat reaction plateau at low pressures, and low cost due to the abundance and facile extraction/processing of Mg.

Hydrogen storage in MH tanks is an exothermic process that produces significant excess heat (in the range of 40–80 kJ mol^{-1} for most materials tested in the literature). Unless the produced excess heat is removed, it results in increasing tank temperatures that eventually satisfy the activation energy barrier for H_2 desorption, and thus the material can no longer absorb more hydrogen leading to incomplete tank chargings. The design of efficient cooling systems for MH tanks is thus a crucial factor for exploiting the maximum theoretical storage capacity of the material.

Hydrogen desorption, on the other hand, is an endothermic reaction that requires sufficient heat fluxes to be provided to the MH bed in order to maintain the desired desorption mass fluxes. Attempts to develop integrated, self-sustainable systems, where the excess thermal power produced from fuel cells under normal operating conditions is redirected towards an MH tank to sustain H_2 desorption have been recently reported. Most of these works have focused primarily on the thermal coupling between low temperature MH tanks and Polymer Electrolyte Membrane (PEM) fuel cells, where the cooling air flow stream from the fuel cell is used to heat the MH tank [4,5].

For high temperature MH materials, such as MgH_2 that exhibits high thermodynamic stability (requiring ~74 kJ mol^{-1} of desorbed H_2) and high activation energy (desorption kinetics are sufficiently fast at temperatures $T \geq 300\ ^\circ C$), thermal coupling is only feasible with high temperature fuel cells, such as Solid Oxide Fuel Cells (SOFC) that typically operate at temperatures above 600 $^\circ C$. For such a combination of high temperature MHs coupled with SOFCs, different heating solutions have been considered so far, including the after-burning of unused H_2, and the electrical heating of the MH tank [6]. However, the design of a self-sustainable, integrated, high temperature SOFC/MH tank system that can efficiently maintain H_2 desorption, until the tank becomes practically fully depleted, still remains an open scientific and engineering problem.

In this work, we propose such an integrated system design where a MgH_2 multiple tank system is heated through radiation and conduction by a SOFC operating at a typical 500 W electrical power. We study the energy balance between the SOFC and the storage system, and derive analytical expressions for the thermal power produced during SOFC operation and the corresponding thermal power required for H_2 desorption from the tanks, as a function of the fuel utilization rate, the SOFC operating temperature and efficiency, and the MH enthalpy of desorption. Based on these calculations, we develop a mathematical model that accounts for heat transfer in the integrated system, as well as mass transfer and desorption kinetics in the tanks, and solve for the dynamics of the coupled system at typical operating conditions and different fuel utilization rates. Our results focus primarily on tank operating conditions, such as tank pressure, temperature and H_2 saturation profiles vs operation time.

2. Solid Oxide Fuel Cell energy balance

SOFCs are electrochemical devices that efficiently convert the Gibbs Free Energy of hydrogen oxidation directly to electrical work. They are constructed by an ion conducting, gas-tight ceramic membrane (typically yttria-stabilized zirconia (YSZ)), that acts as an electrolyte, sandwiched between two porous gas diffusion electrodes (GDE) with both ionic and electronic conductivity [7,8]. Due to the high electrical resistivity of such ceramic materials at room temperatures, SOFCs typically operate at temperatures above 600 $^\circ C$, where YSZ exhibits increased ionic conductivity. In fact, Joule heating at the ceramic electrolyte is the primary source of energy dissipation in SOFCs, as shown in Appendix A.

Hydrogen oxidation occurs at the three-phase boundary (TPB: porous space-ionic conductive material-electronic conductive material) of the anode GDE;

$$H_2(g) + O^{2-} \rightarrow H_2O(g) + 2e^- \tag{1}$$

The electrons produced at the TPB are then transferred over the external circuit towards the cathode GDE, where oxygen is reduced to ions;

$$O_2(g) + 4e^- \rightarrow 2O^{2-} \tag{2}$$

The ions are then in turn transferred towards the anode through the electrolyte to support the first reaction.

The overall reaction is strongly exothermic with an enthalpy change approximately equal to $\Delta H_f = -250$ kJ mol^{-1} (standard enthalpy of water formation). However, given that the entropy of the system is reduced during water formation, only part of this energy is available for producing electrical (non-expansion) work according to the change of the Gibbs Free Energy $\Delta G = \Delta H - T\Delta S$ under isothermal conditions.

From a thermodynamic point of view, the reaction energy that can be used to produce electrical work as a function of the reacting species concentration at the anode and cathode TPBs is described by;

$$\Delta G = \Delta G_0 + RT \ln\left(\frac{\widehat{P}_{H_2O,a}}{\widehat{P}_{H_2,a}\widehat{P}_{O_2,c}^{1/2}}\right) \tag{3}$$

where $\widehat{P} = P/P^0$ is the partial pressure of the species normalized with the standard pressure $P_0 = 1$ atm that corresponds to ΔG_0. The associated reversible Fuel Cell potential is then given by the well-known Nernst equation;

$$E_r = E_0 - \frac{RT}{2F}\ln\left(\frac{\widehat{P}_{H_2O,a}}{\widehat{P}_{H_2,a}\widehat{P}_{O_2,c}^{1/2}}\right) \tag{4}$$

where $\Delta G = -zFE$, $z = 2$ is the number of electron moles exchanged per H_2 mole, and F is Faraday's constant.

In principle, the maximum energy conversion predicted by Eqs. (3) and (4) is never achieved due to irreversibilities in the fuel cell associated with the diffusion and mixing of species in the GDE's, ohmic resistances in the electrodes and the electrolyte, and the activation energies of the reaction kinetics. Due to these effects, part of the Gibbs Free Energy of Eq. (3) is irribsly converted to heat. These irreversibilities (typically termed overpotentials, namely, concentration V_c, ohmic V_o, and activation V_a, respectively) are manifested by reducing the Nernst potential E_r (which corresponds to the maximum theoretical voltage of the SOFC) and are increasing functions of the current density in the fuel cell;

$$E(i) = E_r - V_o(i) - V_c(i) - V_a(i) \tag{5}$$

A sample calculation of the overpotentials based on a mathematical model developed by Zhu et al. [9] for a typical 2D planar SOFC cell is included in Appendix A. This analysis demonstrates that ohmic overpotentials in the electrolyte are the primary source of energy dissipation in SOFCs operating at maximum electrical power. This is an expected result, since both the electric conductivity of GDEs is relatively high, and the activation/concentration

overpotentials are negligible at maximum electrical power (namely at medium current density). Furthermore, at such elevated temperatures the activation barrier of the electrochemical reactions is easily overcome, leading also to negligible activation overpotential effects.

Based on this simplification, we can obtain analytical expressions for the energy balance in an integrated SOFC/MH system as a function of operating temperatures, fuel utilization, enthalpy of desorption and the temperature of the exhaust gases exiting to the environment. Denoting by $\dot{n}$ the molar flow rate of H_2 from the tank to the SOFC anode and by α the mole fraction of H_2 that actually reacts (utilization ratio), the chemical power, $\dot{W}_{ch}$, produced in the SOFC is expressed as follows;

$$\dot{W}_{ch} = \alpha\dot{n}\left|\Delta H_f\right|. \tag{6}$$

A fraction η of this power corresponds to the produced electrical power $\dot{W}_{el}$ and the remaining corresponds to the thermal power $\dot{Q}_{th}$ that can be used to heat the MH tanks;

$$\dot{W}_{el} = \eta\alpha\dot{n}\left|\Delta H_f\right|, \tag{7}$$

and

$$\dot{Q}_{th} = (1-\eta)\alpha\dot{n}\left|\Delta H_f\right|. \tag{8}$$

Part of the produced thermal power is typically used for preheating the reactants to the reaction temperature (namely, the SOFC stack operating temperature). If air is used as the oxidating agent injected at the cathode at stoichiometric analogy to the H_2 molar flow rate, the required power for heating the reactants is;

$$\dot{Q}_{heat} = \dot{n}q_{heat}, \tag{9}$$

where

$$q_{heat} = \int_{T_0}^{T_{op}} \left(c_{p,H_2} + 0.5c_{p,O_2} + 2c_{p,N_2}\right)\mathrm{d}T, \tag{10}$$

and T_{op} is the fuel cell operating temperature, $c_{p,i}$ the heat capacity under constant pressure of component i, and T_0 the initial temperature of the reactants at the inlet stream.

This can be further generalized by considering that H_2 is supplied at a higher temperature than the rest of the reactants, equal to the average operating temperature of the MH tank, T_{tank};

$$q_{heat} = \int_{T_{tank}}^{T_{op}} c_{p,H_2}\mathrm{d}T + \int_{T_0}^{T_{op}} \left(0.5c_{p,O_2} + 2c_{p,N_2}\right)\mathrm{d}T. \tag{11}$$

At the same time, the heat power required to sustain H_2 desorption from the MH tank is;

$$\dot{Q}_{des} = \dot{n}|\Delta H_{des}|, \tag{12}$$

where ΔH_{des} is the enthalpy of H_2 desorption at the tank operating temperature.

Besides the thermal power $\dot{Q}_{th}$ produced at the SOFC, part of the thermal power contained in the outlet stream of the reaction products (exhaust gases) can be also used for heating either the MH tank, or for preheating the reactants inlet. Assuming that the products of the reaction exit from the SOFC to the environment at a temperature equal to T_1, the usable thermal power in the exhaust gases stream is;

$$\dot{Q}_{exh} = \dot{n}q_{exh}, \tag{13}$$

where

$$q_{exh} = \int_{T_1}^{T_{op}} \left[\alpha c_{p,H_2O} + 0.5(1-\alpha)c_{p,O_2} + (1-\alpha)c_{p,H_2} + 2c_{p,N_2}\right]\mathrm{d}T, \tag{14}$$

Furthermore, heat can be also produced using part of the electrical power $\dot{W}_{el}$ of the SOFC when all other heat sources cannot satisfy the heat flux for H_2 desorption from the MH and for preheating the reactants in the SOFC. Assuming that a fraction γ of the produced power is used from joule heating, then the produced thermal power is;

$$\dot{Q}_j = \gamma\dot{W}_{el}, \tag{15}$$

and

$$P_{el} = (1-\gamma)\dot{W}_{el} \tag{16}$$

is the remaining usable electrical power.

The operation of the SOFC is thus sustainable (reaches a steady state) when its temperature remains constant at T_{op} and the following relation is satisfied;

$$\dot{Q}_{th} + \dot{Q}_{exh} + \dot{Q}_j + \dot{Q}_{env} - \dot{Q}_{heat} - \dot{Q}_{des} = 0, \tag{17}$$

where $\dot{Q}_{env}$ is the heat power emitted to the environment in the form of waste heat. In the above notation, the SOFC is heated by an external source when $\dot{Q}_{env} > 0$, and cooled by the environment when $\dot{Q}_{env} < 0$.

Denoting $q_{env} = \dot{Q}_{env}/\dot{n}$ we then take;

$$(1-\eta)\alpha + q_{exh} + q_{env} - q_{heat} - q_{des} = 0. \tag{18}$$

From Eqs. 6–17 and given that $\dot{Q}_{th} = \dot{W}_{ch} - \dot{W}_{el}$, we have;

$$\alpha((\gamma - 1)\eta + 1)\left|\Delta H_f\right| - |\Delta H_{des}| + q_{exh} - q_{heat} = -q_{env} \tag{19}$$

Net energy is released to the environment when $\dot{Q}_{env} \leq 0$, which leads to;

$$\alpha((\gamma - 1)\eta + 1)\left|\Delta H_f\right| - |\Delta H_{des}| + q_{exh} - q_{heat} \geq 0 \tag{20}$$

Note that in the above analysis no assumption has been made regarding the efficiency of the SOFC, namely which fraction of the useful chemical power is converted to electrical. Such an approximation can be made by taking into account that both concentration and activation overpotentials are negligible compared to ohmic overpotentials when the SOFC operates at its maximum power $\dot{W}_{el}$, as shown in Appendix A. Under these conditions the electrical power of the SOFC is;

$$\dot{W}_{el} = EI = (E_r - V_o)I = E_rI - I^2r, \tag{21}$$

where r is the ohmic resistance of the electrolyte, I the current that passes through the circuit, E_r the open circuit voltage of the SOFC (see Eq. (5)) and $\dot{W}_{el,r} = E_rI = \alpha\dot{n}\left|\Delta G_f\right|$ is the maximum reversible electrical power that can be produced by the SOFC, neglecting irreversibilities. The actual peak electrical power of the SOFC is then obtained at;

$$\frac{d\dot{W}_{el}}{dI} = E_r - 2Ir = 0 \qquad (22)$$

Namely, the peak power is;

$$\dot{W}_{el,max} = \frac{E_r^2}{4r}. \qquad (23)$$

at $I_{max} = E_r/2r$. The SOFC efficiency can be thus calculated at I_{max} as follows;

$$\eta = \frac{\dot{W}_{el,max}}{\dot{W}_{ch}} = \frac{\dot{W}_{el,max}}{\dot{W}_{el,r}} \frac{|\Delta G_f|}{|\Delta H_f|} = \frac{E_r^2/4r}{E_r^2/2r} \frac{|\Delta G_f|}{|\Delta H_f|} = 0.5 \frac{|\Delta G_f|}{|\Delta H_f|} \qquad (24)$$

Given thus a typical SOFC efficiency $\eta = 0.5 |\Delta G_f|/|\Delta H_f|$, we can determine the lowest utilization ratio of H_2 in the SOFC to ensure the release of net energy in an integrated SOFC/MH system for typical operating conditions and assuming MgH_2 as a hydrogen storage material. By combining Eq. (20) with Eqs.10 and 11, and setting $T_0 = 300$ K, $T_{tank} = 600$ K, $T_{op} = 1000$ K, $\Delta H_{des} = 75$ kJ mol^{-1}, $\Delta G_f = -200$ kJ mol^{-1} (calculated at T_{op}), $\Delta H_f = -250$ kJ mol^{-1} and the heat capacities of H_2, O_2, N_2, and $H_2O(g)$ referred by NIST [10], we deduce that the lowest utilization ratio for net energy production must be $\alpha \geq 0.73$, when none of the electrical power at the SOFC is used for heating the MH, namely when $\gamma = 0$. In the opposite case, where all the chemical power of H_2 oxidation is irreversibly converted to heat in the SOFC, namely when $\gamma = 1$ (or equivalently when $\eta = 0$), the minimum fuel utilization ratio for net energy production is $\alpha \geq 0.43$.

3. Integrated system design

The above analysis demonstrates that thermal coupling in integrated SOFC/MH tank systems is possible in terms of the available thermal power, even in the case of MHs with high enthalpies of formation (such as MgH_2), provided a high hydrogen utilization ratio of $\alpha \geq 0.73$. Additional analysis, however, is required in order to study the dynamics of integrated systems in terms of heat/mass transfer and H_2 desorption kinetics, and ensure the operating conditions where heat transfer from the SOFC to the MH tank occurs fast enough to maintain both a constant H_2 feed to the SOFC and steady state tank operating conditions (i.e. practically constant tank pressure and temperature).

To this end, we develop a mathematical model that describes heat transfer in the form of radiation and conduction from the SOFC towards the MH tank, and heat and mass transfer within the MH tank itself during H_2 desorption at constant demand. The kinetics of H_2 desorption are described by a first-order reaction, where the reaction rate and activation energy are obtained by a least-square fit on experimental desorption data from the literature [11]. The mathematical model is then solved in 2D (assuming significantly higher gradients in the radial than the axial dimension of the tank) using COMSOL Multiphysics 4.3 finite element software package for the coaxial system design shown in Fig. 1.

Fig. 1 shows only one quarter of the entire system, which is built around a cylindrical SOFC, 0.1 m in diameter and 0.1 m in length. The SOFC is surrounded by a thick stainless steel ring that contains [16] equally spaced MH cylindrical tanks 0.04 m in diameter and 0.1 m in length each. The SOFC and the metal ring are seperated by an air-filled region 0.07 m in thickness that acts as a low conductivity barrier between the SOFC and the MH tanks. The dimensions and operating conditions are based on a commercially available Almus Ubocell SOFC model capable of 500 W electrical power [12].
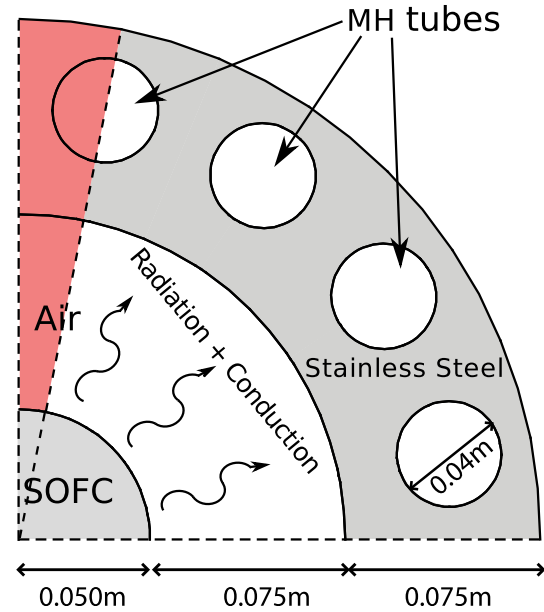

Fig. 1. Schematic of the integrated SOFC/MH system considered in this study. Only one quarter of the total system, that consists of 16 MH tanks in total, is shown here. The computational domain is highlighted with red color. Heat is transferred from the SOFC, that operates at $T = 1000$ K, to the inner surface of the metal ring primarily by radiation. The ring serves to minimize temperature gradients around the tanks and provide uniform desorption patterns, while the air layer blocks heat transfer by conduction, so that the tanks operate at significantly lower temperature than the SOFC. (For interpretation of the references to color in this figure legend, the reader is referred to the web version of this article.)

This particular design is selected in order to take advantage of the radiant heat fluxes from the SOFC to the surrounding MH tanks, while maintaining a significantly lower operating temperature for the tanks (typical operating temperature for the tanks 300 °C $\leq T \leq$ 400 °C, while the typical operating temperature of the SOFC is well above 600 °C) by introducing the low conductivity air layer between the SOFC and the metal ring. This allows for reduced operating pressures within the tanks and minimizes aging of the MH material, while assuring sufficiently fast desorption kinetics. Furthermore, the metal ring surrounding the tanks allows for highly conductive heat transfer around the tanks that produces uniform temperature profiles at the tank walls and thus uniform H_2 profiles within the tanks.

4. Heat transfer between the SOFC and the tanks

The radiant heat flux from the walls of the SOFC stack to the internal perimeter of the metal ring, S, of the porposed integrated design is a function of temperatures of the SOFC and the metal surface of the ring and the emissivity of the materials [13,14];

$$q_{fc} = \frac{1}{\frac{1}{\varepsilon_{fc}} + \frac{A_{fc}}{A_{tank}}\left(\frac{1}{\varepsilon_{tank}} - 1\right)} \sigma\left(T_{fc}^4 - T_{tank}^4\right) \qquad (25)$$

where A_{fc} is the external surface area of the fuel cell, A_{tank} the internal surface area of the surrounding ring which faces the fuel cell, ε_{fc}, ε_{tank} are the emissivity coefficients of the SOFC and tank surfaces, respectively, and σ is the Stefan−Boltzmann constant.

The continuity of heat fluxes at the internal perimeter, S, of the ring then reads;

$$\vec{n} \cdot (k_s \nabla T|_{S_+} - k_a \nabla T|_{S_-}) = q_{fc} \tag{26}$$

where k_s, k_a are the metal and air thermal conductivity, respectively, and $\vec{n}$ is the unit vector normal to the surface, pointing from the metal ring towards the air layer.

Similarly, the conservation of heat within the air layer and the metal ring reads;

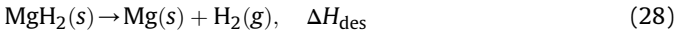$$\rho_i C_{pi} \frac{\partial T}{\partial t} + \nabla \cdot (k_i \nabla T) = 0 \tag{27}$$

where $i = s,a$ (s for steel and a for air) and ρ_i is the density and C_{pi} is the specific heat capacity of the medium, respectively.

In the following simulations, we take $\varepsilon_{fc} = \varepsilon_{tank} = 0.05$, $k_a = 0.08$ W/(m K), $C_{pa} = 1075$ J/(kg K) for air, and $k_s = 24$ W/(m K), $C_{ps} = 475$ J/(kg K), and $\rho_s = 7700$ kg m^{-3} for the metal ring. The above are average values at $T = 700$ K, while the air density is calculated by the ideal gas law at 1 atm pressure.

5. Metal hydride tank modeling

In our simulations, we consider that the cylindrical tanks are filled with MgH$_2$ powder which is a very attractive hydrogen storage medium due to its high storage capacity that ideally may reach up to 7.6% w/w, and thus results in high energy densities. MgH$_2$ however exhibits significant thermodynamic stability and high activation energy for desorption, thus resulting in high tank operating temperatures (300 °C $\leq T \leq$ 400 °C). This latter characteristic makes it an ideal candidate for coupling with high temperature SOFCs.

The MgH$_2$ powder desorbs hydrogen according to the following reaction;

$$\text{MgH}_2(s) \rightarrow \text{Mg}(s) + \text{H}_2(g), \quad \Delta H_{des} \tag{28}$$

where $\Delta H_{des} > 0$ is the heat of the endothermic reaction which is ~74 kJ mol^{-1} at standard state conditions.

The mass balance for H$_2$ in the gaseous phase (void space) of the MH bed reads;

$$\frac{\partial \widehat{\rho}_g}{\partial t} + \nabla \cdot (\rho_g \langle \vec{u} \rangle) = -\widehat{m} \tag{29}$$

where

$$\langle \vec{u} \rangle = -\frac{k}{\mu_g} \nabla P_g \tag{30}$$

where $\widehat{\rho}_g$ is the H$_2$ gaseous phase mass per unit bed volume, which is related to the H$_2$ density ρ_g through the porosity ε, as $\widehat{\rho}_g = \varepsilon \rho_g$, $\widehat{m}$ is the rate of H$_2$ desorption per unit bed volume, k is the bed permeability, $P_g = \rho_g RT/M_g$ is the viscosity of H$_2$ with a temperature dependence calculated by Sutherland's formula $\mu_g = \mu_0 T_0 + C/T + C(T/T_0)^{3/2}$, $C = 72$ K, $T_0 = 293.85$ K, $\mu_0 = 8.76 \times 10^{-6}$ Pa s, T is the temperature and R is the ideal gas constant. We note here that properties with ˆ are averaged over the bed volume, V_b, (solid and void space) and $\widehat{m} = \dot{n} M_g / V_{bed}$.

Assuming negligible solubility and diffusivity of gaseous H$_2$ in the solid phase (MgH$_2$ + Mg mixture) [15], the mass balance for H$_2$ in the metal hydride reads;

$$\frac{\partial \widehat{\rho}_{HS}}{\partial t} = \widehat{m} \tag{31}$$

where $\widehat{\rho}_{HS}$ is the volume averaged concentration of chemisorbed H$_2$ in the bed, which is related to the concentration per unit solid volume as $\widehat{\rho}_{HS} = (1 - \varepsilon)\rho_{HS}$.

For heat transfer, we consider the bed as a homogeneous and isotropic effective continuum, where the thermal properties are averaged over the entire solid and void space and convective heat transfer is neglected;

$$\rho_b C_{pb} \frac{\partial T}{\partial t} + \nabla \cdot (-K_e \nabla T) = \widehat{m} \Delta H_{des} \tag{32}$$

where ρ_b is the bed density, ρ_{MgH_2} is the density of the metal hydride, ε^0 is the initial bed porosity at maximum absorption, C_{pb} is the bed specific heat capacity, K_e is the effective thermal conductivity of bed, and ΔH_{des} is the heat of H$_2$ desorption. The bed density is a function of the absorbed H$_2$ mass fraction $\beta = \widehat{\rho}_{HS}/\widehat{\rho}_{HS,sat}$ as

$$\rho_b = \rho_{MgH_2}(1 - \varepsilon^0)\left(1 - \frac{M_{H_2}}{M_{MgH_2}}(1 - \beta)\right), \qquad \text{where}$$

$\widehat{\rho}_{HS,sat} = (1 - \varepsilon^0)\frac{M_{H_2}}{M_{MgH_2}}\rho_{s,sat}$ is the maximum concentration of absorbed H$_2$. It is then straightforward to show that the bed porosity is $\varepsilon = 1 - \rho_b/\rho_s$, where $\rho_s = \rho_{Mg} + \beta(\rho_{MgH_2} - \rho_{Mg})$ is approximated by a linear interpolation between the densities of pure magnesium and pure MgH$_2$.

The enthalpy of desorption is related to the standard heat of MgH$_2$ formation, ΔH_0, as;

$$\Delta H_{des} = -\Delta H_0 + \int_{298K}^{T} \left(c_{p,Mg} + c_{p,H_2} - c_{p,MgH_2}\right) dT \tag{33}$$

where $c_{p,Mg}, c_{p,H_2}$, and c_{p,MgH_2}, are the specific molar heat capacities of Magnesium, H$_2$ and MgH$_2$, respectively. Assuming an average desorption temperature of $T = 300$ °C, we calculate an average value for the heat of desorption $\Delta H_{des} = 77.9$ kJ mol^{-1} which is used in this study.

It should be noted that the effective conductivity of the bed depends strongly on the particle size distribution of the metal hydride powder, ranging from 2 to 8 W m^{-1} K^{-1} for unmilled and mildly ball-milled powders with particle sizes in the order a few micrometers, to 0.1–1 W m^{-1} K^{-1} for nanoparticle powders [16,17].

5.1. Kinetics of H$_2$ desorption

We assume first-order reactions kinetics for H$_2$ desorption from MgH$_2$ [18,15];

$$m = \rho_{HS,sat} \frac{d\beta}{dt} = -K_o \exp\left(\frac{-E_a}{RT}\right) \beta \rho_{HS,sat} \tag{34}$$

where E_a is the activation energy and K_o is a rate constant. We should note however that this is merely a first order approximation of the desorption process that may take place in several steps, involving several reaction mechanisms [18].

In order to calculate the activation energy and the desorption rate constant, we apply a least square fit of the integrated Eq. (34) to the experimental data of Cabo et al. [11] who performed desorption measurements in a wide temperature range of 330–390 °C and fitted the respective results to the Avrami–Erofeev equation. These results are consistent with other literature data, i.e. [19,18]. The integrated linear equation is $ln(1 - a) = -Kt$, where $a = 1 - \beta$ and $K = K_o \exp(-E_a/RT)$, where we fit only data in the range $0.2 \leq a \leq 0.8$.

Fig. 2 shows the fitted curves and the experimental points where the slope of the curves expresses $K = K(T)$. The activation energy is found $E_a = 153.8$ kJ mol^{-1} using again a least-square fit for $K(T)$ values on the Arrhenious equation, in very good agreement with values reported in the literature for unmilled and/or mildly ball-milled powders [19,18,20].
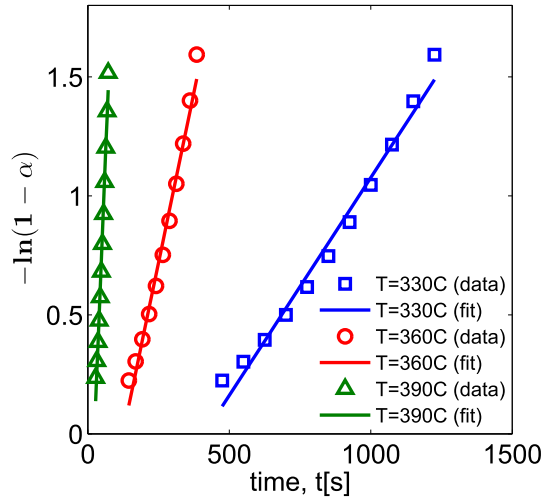
Fig. 2. Kinetics of hydrogen desorption at different temperatures. Points represent experimental data by Cabo et al. [11] and lines are the least-square fitted curves for first order reaction kinetics. The slopes of the curves express the desorption rate constants K as a function of temperature.

Eq. (34) is then modified to account for the effect of H_2 concentration in the void space, which is known to limit desorption at increased pressures [21]. Given that hydrogen absorption is a first-order reaction at least for $T < 340\ °C$ and mild hydrogen pressures [20,21], it is convenient to express the overall desorption/absorption rate per bed volume as;

$$\widehat{m} = -K_0 e^{(-E_a/RT)} \widehat{\rho}_{HS} \left(\frac{P_{eq} - P_g}{P_{eq}} \right) \tag{35}$$

where E_a is the activation energy for H_2 desorption and P_{eq} is the equilibrium pressure of H_2, calculated using Van't Hoff's expression [22]

$$\ln(P_{eq}/P_0) = \Delta H_0/RT - \Delta S_0/R \tag{36}$$

where P_0 is the atmospheric pressure and ΔS_0 is the standard entropy change of the system.

6. Results and discussion

The above mathematical model is solved using COMSOL Multiphysics 4.3 in a computational domain that corresponds to 1/32 (or

$\pi/16$ in cylindrical coordinates) of the entire integrated system (shown in red color in Fig. 1) assuming continuity boundaries in the axial direction. We perform a series of numerical simulations under typical operating conditions of the integrated SOFC/MH system in order to study both the dynamics of the H_2 desorption process and the overall storage system operation for different fuel utilization ratios.

In a typical simulation, we assume that the individual MH tanks and the surrounding space are initially preheated at 350 °C, and we impose a constant temperature $T_{op} = 727$ °C at the perimeter of the SOFC. The external perimeter of the metal ring is thermally insulated, $\vec{n} \cdot \nabla T = 0$, and continuity boundary conditions are applied at the wall of each the MH cylinder.

We then solve the transient model until $t = 3600$ s, while there is no H_2 demand from the MH tanks, as we impose a no flux boundary condition at the wall of each MH cylinder. For times $t > 3600$ s, we impose a constant mass flux, $\dot{N}$, at the wall of each MH cylinder equal to $\dot{N} = \dot{n}/A = \dot{W}_{el}/(32\alpha\eta\pi r_t L\Delta H_f)$, that satisfies the desired electrical power from the SOFC. Here r_t is the tank radius, A is the total surface of the MH tank walls, and we impose $\dot{W}_{el}/L = 5000$W/m (such as the integrated system with a total length of $L = 0.1$ m will produce 500 W electrical power). Simulations are terminated after 2.5 h of tank operation.

Fig. 3 shows the residual H_2 saturation profiles in a single MH tank at four different time steps of applied constant mass flux at a typical $\alpha = 0.8$ fuel utilization in the SOFC. These profiles show that regions closer to tank walls empty faster than regions closer to the tank center, as the local temperature in the former region is expected to be higher thus leading to faster desorption kinetics. This is also evident in Fig. 4 that shows the temperature profiles at the same time steps, rescaled by the maximum and minimum temperatures at each time. The corresponding extreme temperature values are also shown under each profile. These profiles also demonstrate the effect of placing the MH tanks in a highly conductive metal ring, that smooths out temperature gradients at the perimeter of the tanks, thus leading to more or less homogeneous desorption profiles.

Fig. 5(left) shows the residual H_2 saturation profiles in a tank as a function of time for four different utilization ratios. It is apparent that at lower H_2 utilization ratios, the MH tanks empty faster as they need to supply higher mass fluxes to the SOFC, in order to produce a fixed value of electrical power. At the same time, the corresponding heat fluxes entering the tank walls, $\dot{Q}_w/L = (1/L)\int_A [\vec{n} \cdot \nabla(k_s T)]dA$, shown in Fig.5-(right), are significantly higher at lower utilization ratios. Interestingly enough, heat
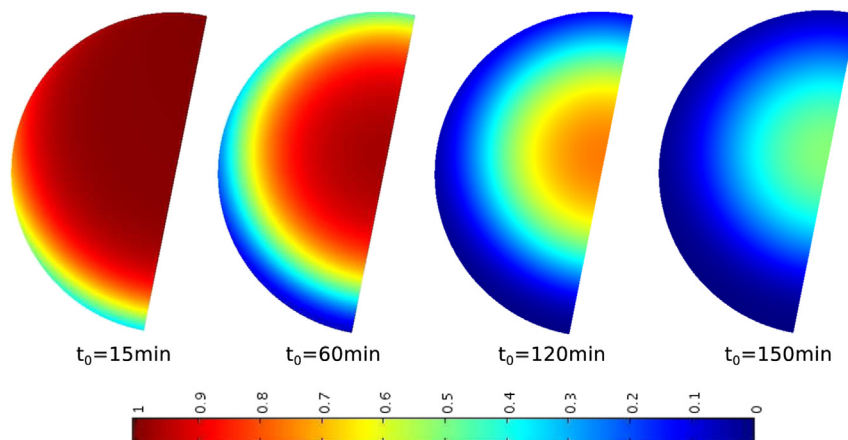

t₀=15min   t₀=60min   t₀=120min   t₀=150min

Fig. 3. Residual H_2 saturation profiles in a single MH tank at four different time steps of applied constant mass flux for $\alpha = 0.8$ fuel utilization ratio. Note that the lower side of the tank is closer to the SOFC walls.
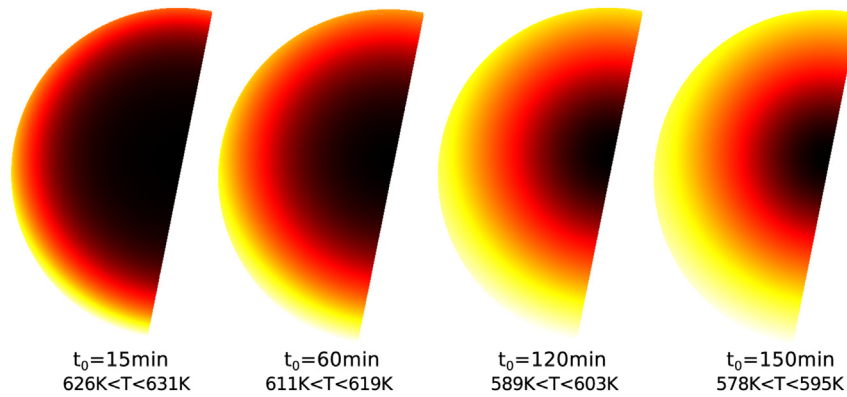
Fig. 4. Temperature profiles in a single MH tank at different time steps of applied constant mass flux for $\alpha = 0.8$ fuel utilization ratio. Note that the lower side of the tank is closer to the SOFC walls.
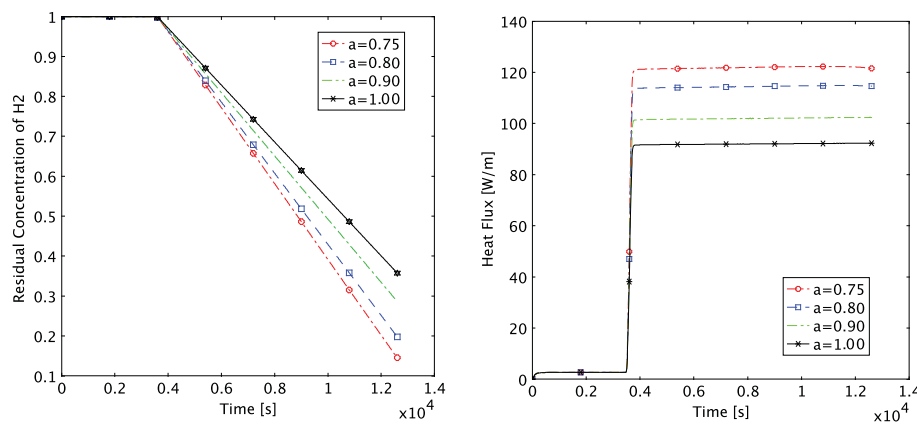

Fig. 5. (Left)-Residual H_2 in the MH tanks vs time, and (Right)-Heat flux normal to tank walls for different fuel utilization ratios.

fluxes appear to reach a steady state value very soon after the application of a constant mass flux boundary condition at the perimeter of the tank under typical operating conditions. It is in fact straightforward to show that the steady-state heat flow rate normal to the tank walls is equal to $\dot{Q}_{des} = \dot{n}\Delta H_{des}$, and by replacing with the imposed mass flux at the tank walls and assuming a typical SOFC efficiency equal to $\eta = 0.5$, we find $\frac{\dot{Q}_{des}}{L} = \left(\frac{\dot{W}_{el}}{\alpha L}\right)\left(\frac{\Delta H_{des}}{\Delta H_f}\right) \cdot \frac{3000}{\alpha}$ W/m. This corresponds to $94/\alpha$ W/m for

the half MH tank of our computational domain, in agreement with the results shown in Fig. 5(right).

Regarding the operating conditions of the MH tank itself, Fig. 6 shows the tank pressure (left) and temperature (right) for the same values of fuel utilization. Assuming that a minimum value of H_2 pressure of ~1 bar is required to be injected to the SOFC anode for the proper operation of the fuel cell, it is apparent that the tanks become quickly pressure depleted at lower fuel utilization ratios, even though there may still be substantial quantities of absorbed H_2. In the case of $\alpha = 0.75$ for example, the tank pressure drops
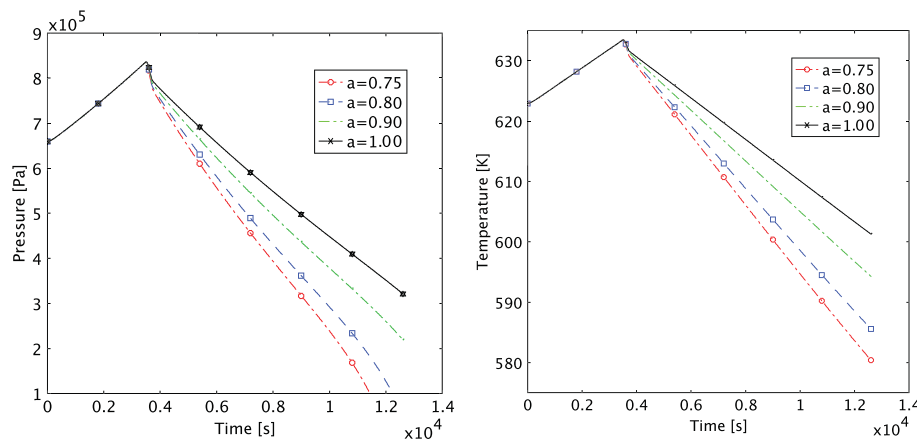

Fig. 6. Dynamics of tank pressure (left) and temperature (right) at different fuel utilization ratios.
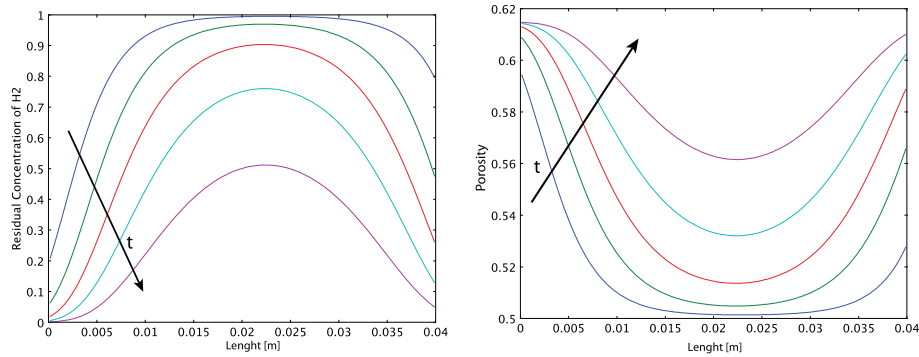
Fig. 7. (Left) Residual H_2 saturation along the diameter of the MH tank at different operation times for $\alpha = 0.8$. Left side of the plot is closer to the SOFC.-(Right) Porosity of the bed at the same times.

below the critical H_2 pressure threshold in less than 2 h of operation, while there still remains 0.25 hydrogen saturation absorbed in the tank. Pressure depletion in the tanks at lower fuel utilization ratios (and thus higher H_2 mass fluxes exiting the tanks) is associated with the poor conductivity of the MH bed (roughly equal to 2 W/(m K)), compared to the excellent conductivity of the surrounding metal medium. Resistance to heat transfer in the tanks also increases significantly with time, as the bed region closer to tank walls becomes progressivelly concentration depleted and desorption proceeds through bed regions closer to the center of the tank (see Fig. 3). Thus the temperature in the central regions drops in order to satisfy the imposed mass and heat fluxes, leading to decreasing tank pressure, as described by the Van't Hoff Equation. It is thus of significant importance to maintain relative small tank radii, in order to avoid early pressure depletion due to the large temperature gradients within the MH tank.

The dynamics of H_2 desorption from the MH tanks are shown in Fig. 7(left) as a function of position along the tank diameter. It is apparent from this plot that the H_2 desorption occurs faster closer to the tank walls, but in a pretty much symmetrical manner. This is due to the presence of the highly conductive metal ring that allows for practically uniform temperatures around the tanks, regardless of the wall distance from the SOFC which is the heat source in this configuration. This is also apparent in Fig. 8 that shows the temperature in the tank and the surrounding metal ring along the diameter of the tank that meets the center of the SOFC at the same time intervals.

An interesting effect of hydrogen desorption from MgH_2 is also demonstrated in Fig. 7-(right) that shows the evolution of the bed porosity along the tank diameter at the same times. Our model predicts an increase of bed porosity with time due to the increasing concentration of Mg in the bed mixture, that has a higher mass density than pure MgH_2 (see also Table 1).

The above results verify that under typical operating conditions a hydrogen utilization ratio of $\alpha > 0.8$, representing the most common value in commercially available SOFCs [23], can ensure the thermal coupling of SOFC and hydrogen storage systems, even in the worst-case scenario of using a metal hydride with a relatively high desorption enthalpy, such as MgH_2. However our approach indicates that coupling can be also achieved with even lower utilization ratios if one considers the use of metal hydrides with appropriate desorption enthalpies. It should be moreover noted that although thermal coupling is mostly appropriate for SOFC systems, the theoretical methodology proposed in this work can be easily adapted to realistically describe a variety of integrated systems, such as the less demanding combination of low temperature hydride storage systems and PEM fuel cells.

7. Conclusions

In this work, we study the thermal coupling potential between a high temperature metal hydride tank and a Solid Oxide Fuel Cell based on principles of SOFC and MH thermodynamics. Given the high operating temperature of SOFCs, we propose a coaxial system design, where the heat power of the SOFC is transferred primarily by radiation and conduction to an assemble of MH tanks, the operating temperature of which is reduced in the region 300−400 °C (allowing fast desorption kinetics for the case of MgH_2, but also several absorption/desorption cycles). Aiming to
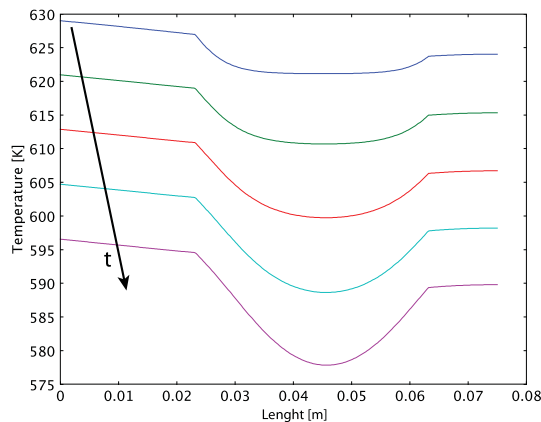

Fig. 8. Temperature of the metal ring and the tank along the diameter at different operation times for $\alpha = 0.8$.

Table 1
Physicochemical properties of bed components [16,17,22,24].

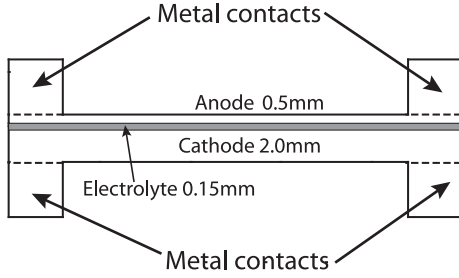| MgH₂ and bed properties	
Pure Mg density, ρ_{Mg}	1739 kg m^{-3}
Pure MgH₂ density, ρ_{MgH_2}	1450 kg m^{-3}
Mixture density, ρ_s	$\rho_{Mg} + \beta(\rho_{MgH_2} - \rho_{Mg})$
MgH₂ molecular weight, M_{MgH_2}	26.3 kg kmol^{-1}
Specific heat capacity of bed, C_{pb}	$(1012.6 + 0.483(T - 273.15) + 530.97\beta)\frac{J}{K \cdot kg}$
Effective thermal conductivity, K_e	2 W/(m·K)
Standard enthalpy of formation, ΔH_0	−74.4 kJ mol^{-1}
Standard entropy change, ΔS_0	−135.1 kJ/(K·mol)
Bed permeability, k	10^{-8} m^2
Initial bed porosity, ε^0	0.5
H₂ properties	
Molecular weight, M_g	2 kg kmol^{-1}
Density, ρ_g	$P_g M_g / RT$
Viscosity, μ_g	Sutherland Formula

Fig. 9. Schematic of the 2D planar, cathode-supported Siemens–Westinghouse type SOFC used in this study. Typical dimensions for the Gas Diffusion Electrodes and the electrolyte are taken by Weber at al [8].

calculate the thermal power required to maintain this particular integrated SOFC/MH configuration self-sustainable, where the heat power produced at the fuel cell is redirected to the MH tanks to trigger/preserve H_2 desorption, we develop a mathematical model that solves for both heat transfer from the SOFC to the MH tanks, and heat/mass transfer within the MH tanks, while accounting for H_2 desorption kinetics from MgH_2. We perform a series of numerical simulations under typical operating conditions to study the dynamics of desorption and the conditions under which the tanks become pressure depleted. Our simulations show that thermal coupling is possible, even for the case of MHs with very high enthalpies of desorption, provided efficiently high fuel utilization ratios at the SOFC. For poorer utilization values, the tanks soon become pressure depleted due to the low thermal conductivity of the MH bed and the resulting sharp decrease in operating temperature, although substantial quantities of H_2 still remain chemisorbed in the MH bed. The proposed approach has a universal nature as it can be also adapted for the coupling of e.g. low temperature hydrides with PEM fuel cells.

Acknowledgments

Appendix A. Modeling SOFC overpotential curves and efficiency

For completeness, we provide the basic theoretical model for the production of electrical power in a simplified 2D planar SOFC design in order to support our argument that ohmic resistances in the ceramic electrolyte membrane is the primary source of energy dissipation in SOFCs operating at peak electrical power resulting in efficiency $\eta \simeq 0.5$.

We consider a cathode-supported Siemens–Westinghouse type fuel cell that consists of an ion-conducting (but gas-tight) ceramic layer, sandwiched between two porous GDEs with both electronic and ionic conductivity (see Fig. 9). Pure hydrogen is supplied by the MH tank at a constant mass flux towards the external surface of the anode GDE and it diffuses through the porous electrode towards the TPB where it reacts with O^{2-} to produce electrons and vapor water (see Eq. (1)). The produced water vapors then counter-diffuse towards the external surface of the anode GDE. By treating the electrode as an effective continuum, mass conservation of H_2 at steady state conditions reads;

$$\nabla \cdot \overrightarrow{J}_{H_2} = \nabla \cdot \left(\rho_{H_2} \overrightarrow{u} + \overrightarrow{j}_{H_2} \right) = r_{H_2} \tag{37}$$

where $\overrightarrow{J}_{H_2}$ is the mass flux of H_2 due to both convection and diffusion in the electrode, $\overrightarrow{u} = \sum \rho_i \overrightarrow{u}_i / \rho$ and $\rho = \sum \rho_i$ is the Darcy velocity and density of the gas mixture (where $i = H_2, H_2O$), respectively, $\overrightarrow{j}_{H_2}$ is the diffusive mass flux, and r_{H_2} is the rate of H_2 consumption at the TPB per unit volume of the GDE.

Assuming that the gas mixture is stagnant, $\overrightarrow{u} = 0$, and the effective diffusivity of H_2, D_{eff}, in the mixture is related to the molecular binary diffusivity, D_m, as $D_{eff} = \varepsilon/\tau D_m$, where $\varepsilon = 0.4$ is the porosity and $\tau = 1.4$ is the tortuosity of the GDE, then mass conservation Eq. (37) takes the following form;

$$\nabla \cdot \left(\rho D_{eff} \nabla \omega_{H_2} \right) = r_{H_2} \tag{38}$$

where $\omega_{H_2} = \rho_{H_2}/\rho$ is the mass fraction of hydrogen.

The rate of hydrogen consumption at the anode can be related to the local current density i_a within the electrode using Faraday's law;

$$r_{H_2} = -\frac{S_a M_{H_2}}{2F} i_a \tag{39}$$

where S_a specific surface of the TPB at the anode, M_{H_2} is the hydrogen molecular weight and F is the Faraday constant.

Similar expressions hold for the mass conservation of species at the cathode GDE, where humified air is supplied at constant mass flux at the external surface of the electrode and diffuses through the electrode, where O_2 is reduced to anions as described by Equation (2). Equation (37) is thus valid for the mass conservation of O_2, but diffusive fluxes are described by the generalized Stefan–Maxwell expressions for a ternary system (namely, H_2O, O_2 and N_2) [24,25]. Thus the diffusive mass flux of O_2 is;

$$\overrightarrow{j}_{O_2} = \rho_{O_2} \sum_{i=1}^{N} \mathbb{D}_{O_2,i} \nabla x_i \tag{40}$$

where x_i is the molar fraction of each species ($i = O_2, N_2, H_2O$) and $\mathbb{D}_{O_2,i}$ are the effective Stefan–Maxwell diffusion coefficients (see Ref. [24] for ternary system expressions) by accounting the effects of porosity and tortuosity in the molecular diffusivities, as above. Note that thermal, pressure and forced diffusion effects are neglected in the above expression [26].

The Darcy velocity of the mixture can be obtained with respect to the N_2 diffusive flux, given that $\overrightarrow{J}_{N_2} = 0$;

$$\overrightarrow{J}_{N_2} = \rho_{N_2} \overrightarrow{u} + \overrightarrow{j}_{N_2} = 0 \Rightarrow \overrightarrow{u} = -\sum_{i=1}^{N} \mathbb{D}_{N_2,i} \nabla x_i \tag{41}$$

The conservation of O_2 then reads;

$$\nabla \cdot \left(\rho_{O_2} \overrightarrow{u} + \overrightarrow{j}_{O_2} \right) = r_{O_2} \tag{42}$$

where the Darcy velocity in the cathode is calculated by Eq. (41), the diffusive mass flux by Eq. (40), and the rate of oxygen reduction can be expressed in terms of the cathode local current density, i_c, as follows;

$$r_{O_2} = -\frac{S_c M_{O_2}}{4F} i_c \tag{43}$$

where S_c specific surface of the TPB at the cathode and M_{O_2} is the oxygen molecular weight.

Table 2
Variables for Butler–Volmer equations.

Anode electrode	
Pre-exponential factor, A_{H_2}	5.59×10^{15} m^2/(s·mol)
Activation energy, $E_{H_2}^{des}$	88.12 kJ mol^{-1}
Site density, Γ	2.6×10^{-5} mol m^{-1}
Sticking coefficient, $S_{H_2}^0$	0.01
Pre-factor for exchange current density, k_{H_2}	2.07×10^9 A m^{-2}
Activation energy for exchange current density, E_{H_2}	87.8 kJ mol^{-1}
Cathode electrode	
Pre-exponential factor, A_{O_2}	4.9×10^{13} Pa
Activation energy, $E_{O_2}^{des}$	H$_2$
Pre-factor for exchange current density, k_{O_2}	5.19×10^8 A m^{-2}
Activation energy for exchange current density, E_{O_2}	88.6 kJ mol^{-1}

The current density produced at the TPB of both the anode and cathode GDEs is typically expressed as a function of the local activation overpotentials V_a at the electrolyte/electrode interface using the Buttler–Volmer equation [27,28]. In this contribution, we adopt the following formalism proposed by Zhu et al. [9,29];

For the anode electrode (hydrogen oxidation);

$$i_a = i_{0,a}\left[\exp\left(\frac{1.5FV_{a,a}}{RT}\right) - \exp\left(\frac{-0.5FV_{a,a}}{RT}\right)\right] \qquad (44)$$

where

$$i_{0,a} = k_{H_2}\exp\left(-\frac{E_{H_2}}{RT}\right)\frac{\left(p_{H_2}/p_{H_2}^*\right)^{1/4}(p_{H_2O}/p^0)^{3/4}}{1+\left(p_{H_2}/p_{H_2}^*\right)} \qquad (45)$$

and

$$p_{H_2}^* = \frac{A_{H_2}\Gamma^2\sqrt{2\pi RTM_{H_2}}}{S_{H_2}^0}\exp\left(-\frac{E_{H_2}^{des}}{RT}\right) \qquad (46)$$

The definitions and values for the variables of the above equations are provided in Table 2.

For the cathode electrode (oxygen reduction);

$$i_c = i_{0,c}\left[\exp\left(\frac{0.5FV_{a,c}}{RT}\right) - \exp\left(\frac{-0.5FV_{a,c}}{RT}\right)\right] \qquad (47)$$

where

$$i_{0,c} = k_{O_2}\exp\left(-\frac{E_{O_2}}{RT}\right)\frac{\left(p_{O_2}/p_{O_2}^*\right)^{1/4}}{1+\left(p_{O_2}/p_{O_2}^*\right)} \qquad (48)$$

and

$$p_{O_2}^* = A_{O_2}\exp\left(-\frac{E_{O_2}^{des}}{RT}\right) \qquad (49)$$

The definitions and values for the variables of the above equations are provided in Table 2.

Assuming a spatially homogeneous TPB in the GDEs, a charge balance for electrons in the electron conductive side of the interface then reads;

$$\nabla\cdot\left(-\kappa_{e,eff}\nabla\varphi_e\right) = Si \qquad (50)$$

where φ_e is the electronic potential, $\kappa_{e,eff}$ is the effective electric conductivity, S is the specific surface area of the GDE equal to S_a for the anode and S_c for the cathode, and i is the current density due to the reaction at the TPB as calculated by Eq. (44) and Eq. (47) for the anode and the cathode, respectively.

A similar charge balance for the oxygen ions in the electrolyte side of the interface reads;

$$\nabla\cdot\left(-\kappa_{i,eff}\nabla\varphi_i\right) = Si \qquad (51)$$

where φ_i is the ionic potential and $\kappa_{i,eff}$ is the effective ionic conductivity of the GDE.

A charge balance in the electrodes (outside the GDEs) reads;

$$\nabla\cdot(-\kappa_e\nabla\varphi_e) = 0 \qquad (52)$$

and for the electrolyte;

$$\nabla\cdot(-\kappa_i\nabla\varphi_i) = 0 \qquad (53)$$

where κ_e and κ_i is the charge conductivity in the electrodes and the electrolyte, respectively.

Eqs. (37)–(53) are solved subject to appropriate boundary conditions using a numerical model developed for COMSOL Multiphysics. Here, we take fixed mass fractions ω for all species at the external surface of the anode and cathode GDE's, and fixed electrical potential E at the external boundaries of the metal electrodes, in order to solve for current production within GDE's and the
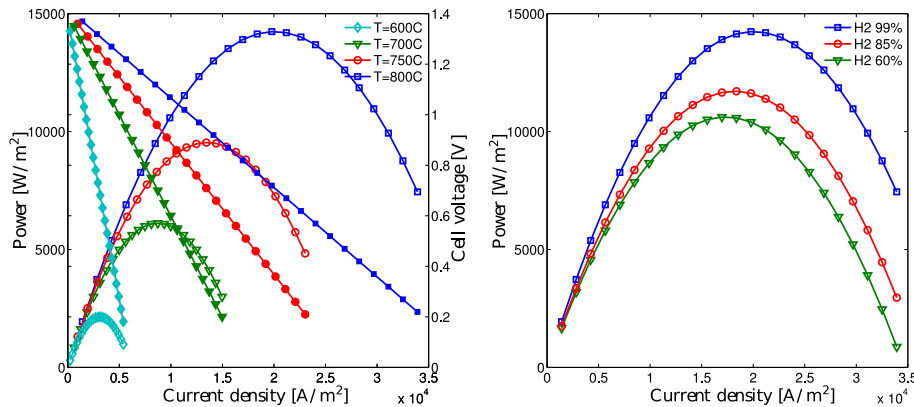

Fig. 10. Effect of operating temperature and H$_2$ molar fraction at the anode inlet on the electrical power (open symbols) and voltage (closed symbols) produced at the SOFC as a function of current density.

species fluxes across the external GDE's boundaries. We use the potential difference E across the electrodes as an independent variable in order to calculate the corresponding current density through the external circuit and the produced electrical power.

The overall current density produced by the SOFC is then calculated at the anode GDE by $I = \frac{S_a}{A}\int_v \dot{i}_a dv$, where A is the surface of the anode GDE open to the H_2 inlet. The produced electrical power is calculated as $\dot{W}_{el} = EI$ and the fuell cell efficient is $\eta = \dot{W}_{el}/\dot{n}\Delta H_f$, where $\dot{n}$ is the calculated mass flux of H_2 entering the anode GDE.

Fig. 10 shows typical polarization curves and the produced electrical power at different SOFC operating temperatures. Interestingly enough, the electrical power curves correspond to a second degree polynomial of current density in agreement with Eq. (22), where the internal resistance of the SOFC perfectly matches that of the ceramic electrolyte layer of the same thickness as a function of temperature. Namely, the electrical conductivity of the electrolyte $k_l = (\sigma/T)\exp(-E_l/(RT))$, where $\sigma = 3.6{\times}10^5$ S K cm^{-1} and $E_l = 8 \times 10^4$ J mol^{-1} [9]. The calculated fuel cell efficiency at peak electrical power is $\eta \simeq 0.5$ at all temperatures.

References

[1] C. Corgnale, B.J. Hardy, D.L. Anton, Int. J. Hydrogen Energy 37 (2012) 14223—14233.
[2] J.M.B. von Colbe, O. Metz, G.A. Lozano, P.K. Pranzas, H.W. Schmitz, F. Beckmann, A. Schreyer, T. Klassen, M. Dornheim, Int. J. Hydrogen Energy 37 (2012) 2807—2811.
[3] M. Jehan, D. Fruchart, J. Alloys Compd. 580 (2013) S343—S348.
[4] B.D. MacDonald, A.M. Rowe, Int. J. Hydrogen Energy 31 (2006) 1721—1731.
[5] B.D. MacDonald, A.M. Rowe, J. Power Sources 161 (2006) 346—355.
[6] B. Delhomme, A. Lanzini, G.A. Ortigoza-Villalba, S. Nachev, P. de Rango, M. Santarelli, P. Marty, P. Leone, Int. J. Hydrogen Energy 38 (2013) 4740—4747.
[7] S. Singhal, Solid State Ionics 135 (2000) 305—313.
[8] A. Weber, E. Ivers-Tiffee, J. Power Sources 127 (2004) 273—283.
[9] H. Zhu, R. Kee, V. Janardhanan, O. Deutschmann, D. Goodwin, J. Electrochem. Soc. 152 (2005) A2427—A2440.
[10] P. Linstrom, W. Mallard, NIST Chemistry WebBook, 20899 edition, National Institute of Standards and Technology, Gaithersburg MD, 2014.
[11] M. Cabo, S. Garroni, E. Pellicer, C. Milanese, A. Girella, A. Marini, E. Rossinyol, S. Suriach, M.D. Bar, Int. J. Hydrogen Energy 36 (2011) 5400—5410.
[12] U. Bossel, ALMUS UBOCELL SOFC Module, April 16, 2014.
[13] J. Lienhard IV, J. Lienhard V, A Heat Transfer Textbook, third ed., Phlogistron Press, Cambridge, Massachusetts, 2003.
[14] D.L. Damm, A.G. Fedorov, J. Power Sources 143 (2005) 158—165.
[15] V. Vons, A. Anastasopol, W. Legerstee, F. Mulder, A. Eijt, A. Schmidt-Ott, Acta Mater. 59 (2011) 3070—3080.
[16] J. Kapischke, J. Hapke, Exp. Therm. Fluid Sci. 17 (1998) 347—355.
[17] Y. Ishido, M. Kawamura, S. Ono, Int. J. Hydrogen Energy 7 (1982) 173—182.
[18] J. Mao, Z. Guo, X. Yu, H. Liu, Z. Wu, J. Ni, Int. J. Hydrogen Energy 35 (2010) 4569—4575.
[19] J. Huot, G. Liang, S. Boily, A.V. Neste, R. Schulz, J. Alloys Compd. 293—295 (1999) 495—500.
[20] J. Fernndez, C. Snchez, J. Alloys Compd. 340 (2002) 189—198.
[21] K. Bohmhammel, B. Christ, G. Wolf, Thermochim. Acta 310 (1998) 167—171.
[22] J. Stampfer Jr., C. Holley Jr., J. Suttle, J. Am. Chem. Soc. 82 (1960) 3504—3508.
[23] Sunfire, Sunfire Integrated Stack Module, April 16, 2014.
[24] R.B. Bird, W.E. Stewart, E.N. Lightfoot, Transport Phenomena, John Wiley & Sons, Inc., 2006. Revised 2nd edition.
[25] C.F. Curtiss, R.B. Bird, Ind. Eng. Chem. Res. 38 (1999) 2515—2522.
[26] S. Whitaker, Rev. Mex. Ing. Quim. 8 (2009) 213—244.
[27] John O'M Bockris, Amulya K.N. Reddy, Maria Gamboa-Aldeco, Modern Electrochemistry 2A: Fundamentals of Electrodics, second ed., Kluwer, 2002.
[28] K.K.S.C. Bockris, High Temperature Solid-oxide Fuel Cells: Fundamentals, Design and Applications, first ed., Elsevier, 2003.
[29] V.M. Janardhanan, O. Deutschmann, J. Power Sources 162 (2006) 1192—1202.